Pharm Res (2014) 31:1426–1437
DOI 10.1007/s11095-013-1021-8

RESEARCH PAPER

CD44 Targeting Magnetic Glyconanoparticles for Atherosclerotic Plaque Imaging

Mohammad H. El-Dakdouki • Kheireddine El-Boubbou • Medha Kamat • Ruiping Huang • George S. Abela • Matti Kiupel • David C. Zhu • Xuefei Huang

Received: 5 September 2012 / Accepted: 4 March 2013 / Published online: 9 April 2013

ABSTRACT

Purpose The cell surface adhesion molecule CD44 plays important roles in the initiation and development of atherosclerotic plaques. We aim to develop nanoparticles that can selectively target CD44 for the non-invasive detection of atherosclerotic plaques by magnetic resonance imaging.

Methods Magnetic glyconanoparticles with hyaluronan immobilized on the surface have been prepared. The binding of these nanoparticles with CD44 was evaluated *in vitro* by enzyme linked immunosorbent assay, flow cytometry and confocal microscopy. *In vivo* magnetic resonance imaging of plaques was performed on an atherosclerotic rabbit model.

Results The magnetic glyconanoparticles can selectively bind CD44. In T2* weighted magnetic resonance images acquired *in vivo*, significant contrast changes in aorta walls were observed with a very low dose of the magnetic nanoparticles, allowing the detection of atherosclerotic plaques. Furthermore, imaging could be performed without significant delay after probe administration. The selectivity of hyaluronan nanoparticles in plaque imaging was established by several control experiments.

Conclusions Magnetic nanoparticles bearing surface hyaluronan enabled the imaging of atherosclerotic plaques *in vivo* by magnetic resonance imaging. The low dose of nanoparticles required, the possibility to image without much delay and the high biocompatibility are the advantages of these nanoparticles as contrast agents for plaque imaging.

KEY WORDS atherosclerotic plaques · CD44 · contrast agents · inflammation · nanoparticles

ABBREVIATIONS

DLS	Dynamic light scattering
ELISA	Enzyme linked immunosorbent assay
FITC	Fluorescein isothiocyanate
FSPGR	Fast spoiled gradient recalled
HA	Hyaluronan
IL	Interleukin
LDL	Low density lipoprotein
mAb	Monoclonal antibody
MRI	Magnetic resonance imaging
NPs	Nanoparticles
ROI	Region of interest
siRNA	Small interfering RNA
SPION	Superparamagnetic iron oxide nanoparticle
TEM	Transmission electron microscopy
TNF-α	Tumor necrosis factor-α

INTRODUCTION

Cardiovascular diseases, which are associated with atherosclerosis, are the leading causes of morbidity and

Electronic supplementary material The online version of this article (doi:10.1007/s11095-013-1021-8) contains supplementary material, which is available to authorized users.

M. H. El-Dakdouki • K. El-Boubbou • M. Kamat • X. Huang (✉)
Department of Chemistry Michigan State University
Chemistry Building, Room 426, 578 S. Shaw Lane
East Lansing, Michigan 48824, USA
e-mail: xuefei@chemistry.msu.edu

R. Huang • G. S. Abela
Department of Medicine, Division of Cardiology
Michigan State University
East Lansing, Michigan 48824, USA

M. Kiupel
Department of Pathobiology and Diagnostic Investigation
Michigan State University, 4125 Beaumont Road
Lansing, Michigan 48910, USA

D. C. Zhu (✉)
Departments of Radiology and Psychology
Michigan State University, East Lansing
Michigan 48824, USA
e-mail: zhuda@msu.edu

mortality in the world. It is now known that inflammation plays key roles in the pathogenesis of atherosclerotic diseases, which leads to plaque instability and tendency to rupture resulting in heart attacks and strokes (1). Traditionally, diagnosis of atherosclerosis has focused on the detection of severe artery narrowing (stenosis) due to plaque growth towards the lumen. However, unstable vulnerable atherosclerotic plaques often do not narrow the arteries by more than 50%, which are difficult to detect with conventional diagnostic approaches. Serum markers such as C-reactive protein can only provide a gauge on the level of systemic inflammation. Therefore, it is highly desirable that tools can be developed to detect plaques and associated local inflammation.

Magnetic Resonance Imaging (MRI) has emerged as a powerful non-invasive technique to image plaque anatomy. To better evaluate plaque stability, the acquisition of local molecular and biochemical information becomes crucial, which can be aided by contrast agents (2). There are two general classes of contrast agents utilized for molecular imaging of plaques. The first is the Gd based T1 contrast agents (2–9). A potential complication in using Gd, however, is the association of Gd usage in some renal dysfunction patients with the development of nephrogenic systemic fibrosis, an untreatable fatal disease (10). Superparamagnetic iron oxide nanoparticles (SPIONs) are another family of contrast agents being actively developed (11). Typical SPIONs do not bear any targeting agents, and can be internalized by macrophages due to their abilities to non-specifically uptake particulate objects (12). With large concentrations of macrophages in active inflamed plaques, SPIONs can accumulate in these plaques. Magnetic nanoparticles (NPs) such as SPIONs can enhance the transverse relaxation of protons in nearby water, thus causing signal loss and darkening in T2* based MR images and allowing differentiation of plaques from surrounding tissues. However, as the common SPIONs lack inherent affinity towards macrophages, high concentrations of SPIONs (typically 56 mg Fe/Kg body weight in rabbit model. In humans, 2.6 mg Fe/Kg have been used) were generally utilized to ensure sufficient quantities of NPs reached plaque (12–15). Thus, to allow sufficient NP accumulation in plaques and clearance of NPs from the blood pool and the background, imaging was commonly performed at least 1 day and optimally 4 to 5 days after injection (12–16). Furthermore, although SPIONs are generally considered biocompatible (17), there may be safety concerns for longitudinal studies due to the relatively high dose of SPIONs needed (18).

One approach to address the challenges of using SPIONs is to improve their plaque selectivities by immobilizing ligands that can recognize receptors present in plaques (2). Several targeting ligands have been investigated, which include phage display-derived peptide binders and mAb for VCAM (19–21), annexin V for apoptotic cells (22, 23), sulfated dextrans for scavenge receptors (24) and mAb and small molecule ligand for selectin (25, 26). However, in many of these studies, high NP concentrations (3.9–30 mg Fe/Kg) and/or prolonged delay after injection were still necessary for imaging (20, 24). Furthermore, as plaques are complex, it is highly desirable that multiple markers are available for more accurate analysis. This necessitates the continued development of new imaging probes.

Local inflammation plays a key role in both generation of atherosclerotic diseases and plaque rupture (1, 27). Multiple studies have suggested that a cell adhesion molecule CD44 can promote atherosclerosis by mediating inflammatory cell recruitment to plaques and vascular cell activation (28–30). CD44 is expressed on the surface of major cell types present in the atherosclerotic plaques including vascular endothelial cells, macrophages and smooth muscle cells (30–34). In an atherosclerotic mouse model the apolipoprotein E knockout mice, it was reported that CD44 expression varied in vascular vessels and was highest at lesion prone sites (29, 30). This was corroborated in human studies where CD44 was present in rupture-prone macrophage-rich regions of human atherosclerotic plaques at a level over 10 times higher than that in healthy vascular tissues (31, 35, 36). CD44 was also found over-expressed in atherosclerotic rabbits (37). The elevated CD44 expression correlated with a 10 fold enhancement in the secretion of proinflammatory cytokines such as interleukin-1β (IL-1β) and IL-6 from endothelial cells and macrophages and these cytokines in turn augmented CD44 expression (31, 35). Such a positive feedback loop can exacerbate atherosclerosis leading to plaque instability. Knocking out CD44 in ApoE knockout mice led to 50~70% reduction in aortic lesions as well as 90% fewer macrophages present in the lesions (30). Furthermore, gene expression profiling of aortas from CD44 knockout mice compared with their CD44 wild-type counterparts led to the discovery that CD44 regulates focal adhesion formation, extracellular matrix deposition and angiogenesis, processes critical to atherosclerosis (29). These data established the important roles of CD44 in plaque initiation and development. However, CD44 has not been investigated as a target for molecular imaging of atherosclerotic plaques.

The principle endogenous ligand of CD44 is hyaluronan (HA), a naturally existing polysaccharide comprised of tandem disaccharide repeats of β-1,4-D-glucuronic acid-β-1,3-D-N-acetylglucosamine (38, 39). Although CD44 can also be found on non-plaque residing cells, HA and CD44 interactions are subject to tight regulation. CD44 is normally maintained in a quiescent state showing little appreciable HA binding (40). For example, freshly isolated peripheral

blood monocytes and lymphocytes are known to express CD44, but they do not bind HA (41). During inflammation, however, the pro-inflammatory cytokine tumor necrosis factor-α (TNF-α) induces sulfation of CD44 and causes subsequent conformational changes, which transform CD44 into the high HA affinity form (40, 42–44). The non-covalent interaction between *activated and functional* CD44 on endothelial cell surface and HA is sufficiently strong to provide resistance to shear under physiologic conditions and thereby help mediate lymphocyte recruitment (44, 45). The over-expression of CD44 at plaques coupled with the high affinity of CD44 for HA during inflammation renders it attractive to utilize HA/CD44 interactions for plaque imaging.

Herein, we report a biomimetic approach (46) using HA functionalized magnetic NPs to detect atherosclerotic plaques by targeting CD44. There are many advantages in using HA, which include its high biocompatibility, high stability towards chemical modifications and much lower cost compared to antibodies (39). We envision HA functionalized magnetic NPs can serve as mimetics of inflammatory cells and be recruited to plaque sites through CD44 binding. This in turn should enable plaque detection *via* MRI.

MATERIALS AND METHODS

Procedure for Anti-CD44 mAb Staining of CD44 on EA.hy926 Cells

EA.hy926 cells (2×10^5 cells/well) were inoculated in two wells of a 4-well borosilicate plate and incubated for 24 h at 37°C and 5% CO_2. The cells were then fixed using 10% neutral buffered formalin (0.75 ml) for 15–20 min. The cells were washed twice (10 min each) with DPBS containing 0.05% Tween 20 (washing buffer) on an orbital shaker. To one well, PE-Cy^{TM}5 anti-CD44 mAb IM7 (25 μg/ml–1%BSA/DPBS, 200 μl) was added while the other well was used as control where 1% BSA-DPBS (200 μl) was added. The plate was incubated for 3 h at 4°C. After incubation, the wells were washed twice with the washing buffer for 10 min as described above. The wells were then washed with double distilled water for 5 min to avoid PBS crystallization on the sample. Images were collected on an Olympus FluoView 1000 LSM confocal microscope.

Procedure for Western Blot

The supernatant media of EA.hy926 cells in cell culture plates was removed and the cells were washed with ice cold cell culture grade PBS twice. After all the PBS was removed, cold RIPA lysis and extraction buffer (Sigma) was added and the culture plates were gently rocked at 4°C till cell debris started to float (about 10~15 min). The bottom surface of the plate was scraped using a cell scraper. All the liquid on the plate was transferred to a pre-cooled eppendorf tube and sonicated in a bath sonicator (with ice in the bath) for 10 s. The tube was then centrifuged at 4°C for 5 min and the supernatant was separated from the debris. The amount of protein in the supernatant was determined by the Bradford assay. The proteins (20 μg) were separated by SDS-PAGE gel electrophoresis and transferred to a PVDF membrane. The membrane was blocked with 4% milk in TBST (2.43 g/L Trizma, 8.01 g NaCl, pH7.6, 0.1%v/v Tween 20) for 1 h at RT. The blocking solution was decanted and the gel was washed with TBST 3 times. The membrane was then incubated with the mouse antihuman CD44 IgG antibody (primary, 156–3C11, Cell signaling) (1:1000 dilution in 4% milk TBST) at 4°C overnight. The membrane was washed with TBST three times, treated with horse radish peroxidase (HRP) conjugated goat anti-mouse IgG secondary antibody (secondary, BioRad, 1:50,000 dilution in 4% milk TBST) for 1 h at RT and washed again with TBST three times. The washing solution was decanted and a chemiluminescent HRP detection reagent (Denville Scientific) was sprayed onto the membrane followed by development of the autoradiography film. For β-actin detection, the mouse antihuman β-actin peroxidase antibody AC-15 (Sigma-Aldrich, cat # A3854) at the dilution of 1:40,000 was used following the same procedure for CD44 blotting.

HA-NP Uptake by EA.hy926 Cells Using Flow Cytometry and Laser Confocal Imaging

EA.hy926 cells (2×10^5 cells/well) in FBS containing-DMEM medium were inoculated in a 6-chambered plate and incubated at 37°C and 5% CO_2 till the cells became confluent. For study of activated EA.hy926 cells, TNF-α (Human recombinant from Sigma) was added to the culture media to the final concentration of 10 ng/mL and the cells were incubated for another 24 h at 37°C. The supernatant media was removed and the cells were washed with PBS once. Fresh DMEM media was added with FITC-HA-NP and the cells were incubated at 37°C for 24 h more. The cells were then washed with PBS three times and trypsinized with 0.25% trypsin-EDTA (1 mL). Trypsin was neutralized with serum-containing DMEM (5 times), and the cells were collected by centrifugation (500 g). The cells were resuspended in serum-containing DMEM (300 μL) and transferred to FACS tubes. The cells were stored on ice till the time of FACS analysis.

For confocal microscopy analysis, Lysotracker red (1 μM, 50 μL/well) was added 1 h before the end of NP incubation. The supernatant was removed. The cells were washed twice with PBS, and fixed with 10% formalin (1 ml/well) for

15 min. Formalin was removed and the cells were washed twice with PBS. PBS (200 μl/well) and DAPI (300 nM, 300 μl/well) were added, and the cells were incubated for 4–5 min. DAPI solution was removed, and the cells were washed with PBS and water. The plate was covered by an aluminum foil and stored at 4°C till imaging time. Images were gathered on an Olympus FluoView 1000 LSM confocal microscope.

siRNA Knockdown of CD44 in EA.hy926 Cells

EA.hy926 cells were split 1 day prior to the knockdown experiment and cultured. The cells were trypsinized from the culture plate and counted. The cells (1×10^6 cells) were centrifuged at 200×g for 10 min and the pellet was resuspended in nucleofector buffer solution (100 μL). The cells were transferred to the electroporation cuvette carefully using a micropipette followed by addition of 1–10 μM of siRNA. The cuvette was inserted to the electroporator and electroporation of the cells were performed. After completion, media was added to the cuvette. The cells were then transferred to culture plates, incubated and harvested at necessary time points. The expression levels of CD44 were determined by Western blot as described above.

Procedures for Rabbit MRI

All animal experiments were in accordance with the guidelines and the approval of Institutional Animal Care and Use Committee, Michigan State University. New Zealand White rabbits ($n=4$, male, 1 year old, ~ 3 kg body weight) underwent balloon de-enothelialization procedure as follows: the rabbits were anesthetized using ketamine (35 mg/kg, i.m.) and xylazine (5 mg/kg, i.m). A 4 F Fogarty arterial embolectomy catheter (Baxter Healthcare Corp, Irvine, CA) was inserted into the aorta through the right femoral artery of a rabbit. The balloon was then inflated with air (1 mL) and pulled back gently to the ilio-femoral artery junction using an external body measurement of the rabbit. This was repeated three times and the catheter was removed. This procedure was similar to one performed in human patients under local anesthesia and entails minimal stress. The artery was ligated with a suture for subcutaneous and skin closure and local triple antibiotic was put over the wound area. The rabbits were kept warm over a heating pad, observed until they recovered from general anesthesia and then returned to their cages. An antibiotic (enrofloxacin/Baytril 10 mg/kg SQ) was given once pre-operatively to prevent infection. An analgesic, buprenophine (0.01 mg/kg SQ) was given after general anesthesia to avoid additional stress and every 12 h for 48 h following surgery. The rabbits were then fed a cholesterol-enriched diet (1%) for 4 weeks to promote atherosclerotic plaque development.

For MRI, after anesthetization (ketamine 35 mg/kg and xylazine 5 mg/kg IM), the rabbits were held in a supine position on plastic boards with medical tape to minimize motion artifact and placed inside an 8-channel knee coil for MRI. MRI was carried out on a GE 3 T Signa® HDx MR scanner (GE Healthcare, Waukesha, WI). After a 3-plane localizer, a 2D time-of-flight (TOF) pulse sequence was used first to localize the rabbit aorta with the following parameters: Axial scan, anterior-posterior frequency direction, flow compensation, flip angle = 60°, echo time (TE) = 4.4 ms, time of repetition (TR) = 23 ms, receiver bandwidth (rBW) = +/− 15.6 kHz, field of view (FOV) = 14 cm, slice thickness = 2 mm, number of slices = 79, acquisition matrix = 256×128, number of excitation (NEX) = 1, and scan time = 4 min 4 s. Then high-resolution 3D fast spoiled gradient recalled echo (FSPGR) images were acquired to cover the rabbit aorta with the center around the kidney and liver regions with the following parameters: Axial scan, anterior-posterior frequency direction, flip angle = 15°, TE = 13.9 ms, TR = 28 ms, rBW = +/− 5 kHz, field of view = 12 cm, slice thickness = 1 mm, number of slices = 90, acquisition matrix = 256×256, NEX = 2, and scan time = 21 min 34 s. The frequency direction has been set up to minimize the motion artifacts at the aorta.

HA-NPs or the NP 1 (0.21 mg of Fe/kg of body weight in 1 mL sterile saline) were injected through the marginal ear vein of a rabbit. T2*-weighted images acquired with the 3D FSPGR sequence were used to detect the effect of the nanoparticles. To quantify the MR signal changes over time from NP injection, the signal intensities at the aorta wall from the images acquired before injection and after injections were normalized by the mean signal intensity at the back muscle lateral to the spine. Muscle signals provided good calibration of the slight variation of background in images acquired at different time points.

As the animal could not be kept on the scanner under anesthesia for more than 1 h, to compare images acquired at different time points, slice locations were matched through anatomic landmarks (e.g., spinal muscle, renal bifurcation and iliac bifurcation). Anatomic landmarks gave very close but not identical positional match. To avoid the potential bias in image analysis, three consecutive slices (each slice is 1 mm thick) in the location of interests covering 3 mm range were examined. If all these slices showed significant contrast changes compared to pre-injection images, these slices were subject to signal quantification analysis. In the region around kidney and liver, there were usually three to four areas with three or more slices showing significant contrast changes post injection. For signal quantification, a region of interest (ROI) of approximately 4 mm^2 was drawn at the aorta vessel wall to evaluate the intensity changes in T2*-weighted images. At the same slice location, an ROI was drawn at the lumen of

the aorta to evaluate the change of signal intensity in the blood and a reference ROI was drawn at a nearby spinal muscle (thoracolumbar fascia). The mean intensities and standard deviations of these signals were recorded. The intensities at the vessel wall and lumen were calibrated against those from the spinal muscles to minimize the systemic variations. The pre-injection signal intensities of the lumen and the vessel wall were set as 100% respectively. Relative MRI signal intensity changes (%) were calculated using the following formula:

$$\frac{\left(\text{Signal Intensity}_{\text{pre-injection}} - \text{Signal Intensity}_{\text{post-injection}}\right)}{\text{Signal Intensity}_{\text{pre-injection}}} \times 100\%,$$

where the signal intensity had been normalized against the spinal muscle reference ROI. Statistical analysis was performed using a two-tailed student's *t* test.

RESULTS

Our study started from the immobilization of HA on NPs. The superparamagnetic nanoparticles (NP 1), prepared by a modified co-precipitation method (47), were functionalized with amines followed by the attachment of HA (MW ~ 16 kDa) through amide bond leading to HA-NPs (Fig. 1). The NPs obtained were extensively characterized by a variety of techniques including transmission electron microscopy (TEM), dynamic light scattering (DLS), thermogravimetric analysis (TGA), zeta potential, enzyme linked immunosorbent assay (ELISA) and MRI. TEM showed the core size around 6 nm (Fig. S1a). The average hydrodynamic diameters of NPs could be controlled by the amount of dextran used for coating (47). The HA-NPs used in this study had hydrodynamic diameters around 45 nm measured by DLS, which were smaller than those prepared previously (48–50). The smaller NPs can potentially have longer circulation time *in vivo* due to reduced uptake by the reticuloendothelial system (51). The successful attachment of HA on NP was supported by several lines of evidence: 1) TGA data showed that upon heating to 1000°C, the percentage of weight loss due to combustion of NP 1 was 59%, while the percentage from HA-NP increased to 78% (Fig. S1b). Based on this weight loss change, it was calculated that there was 0.46 mg of HA on each mg of HA-NP. The zeta potential of NP 1 was measured to be −2.4 mV and that for HA-NP was - 28.5 mV. The significant increase in the negative value of the zeta potential was presumably caused by the attachment of the negatively charged HA on the NPs. The HA immobilized on HA-NPs maintained its biological recognition. ELISA assay showed that HA-NP could compete with HA for CD44 binding, while NP 1 without HA did not (Fig. S2). The HA-NPs had excellent magnetic relaxivities (r_2* value = 361 mM $^{-1}$s^{-1} at 3 T, Fig. S3), thus were good contrast agents for T2* weighted MRI.

Stability of NPs under physiological conditions is critical in order to avoid harmful particle agglomeration in the presence of serum proteins *in vivo*. The HA-NPs maintained their sizes in both PBS buffer and culture media containing 10% fetal bovine serum (FBS) over 1 week, demonstrating that serum proteins did not induce NP aggregation and the particles had excellent colloidal stabilities (Section S5, Fig. S4).

Traditionally, macrophages have been the primary focus in atherosclerotic plaque detection studies (12–15). Previously, we have shown that macrophages can selectively uptake HA-NPs in a CD44 dependent manner (48). The interior surface of vascular vessels is lined with vascular endothelial cells, which are likely the first plaque residing cells in contact with NPs in circulation. Furthermore, endothelium dysfunction is a hallmark of atherosclerosis (52). These considerations prompted us to examine the interactions of HA-NPs with the human vascular endothelial cells EA.hy926 (53) as an *in vitro* model of vascular endothelium. EA.hy926 cells express CD44 on the cell surface as shown by immunostaining with an anti-CD44 mAb (Fig. 2a), which was further confirmed by Western blot (Fig. 2b). As a control, LNCaP cells, which express little CD44 (54, 55), did not get stained with anti-CD44 mAb.

To evaluate cellular interactions of NPs by fluorescence, the fluorophore fluorescein isothiocyanate (FITC) was introduced onto HA-NPs through thiourea bond formation producing FITC-HA-NPs. Control particles without HA (FITC-NPs) were produced in a similar manner. The NPs were incubated with EA.hy926 cells for 24 h at 37°C followed by thorough washing to remove unbound particles. Flow cytometry analysis was then carried out to determine the amounts of NPs bound to the cells. Although EA.hy926 cells express CD44, they did

Fig. 1 Synthesis of HA-NPs.

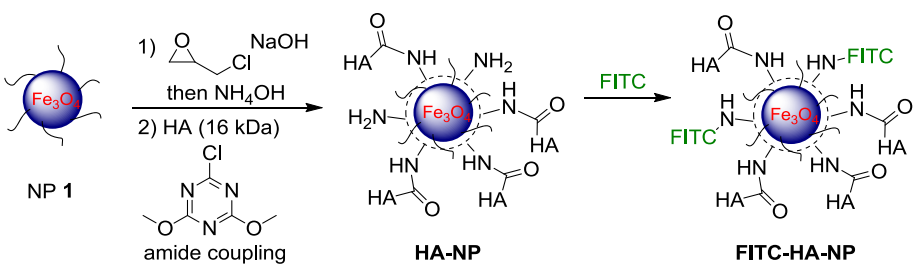

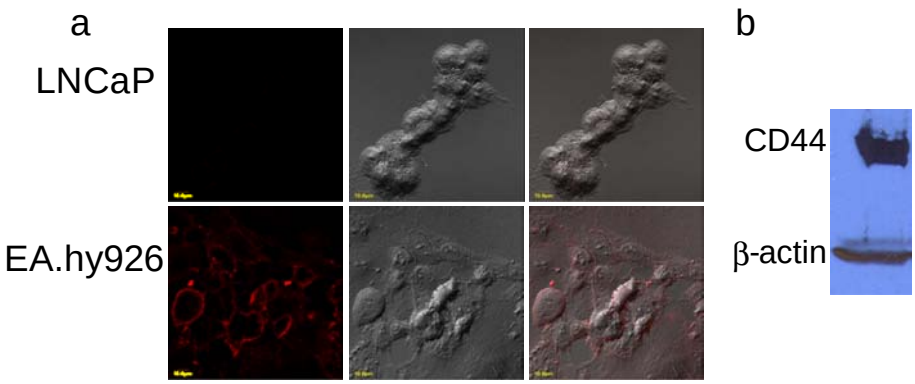

Fig. 2 (**a**) Anti-CD44 mAb IM7 staining of CD44 on EA.hy926 cells imaged by confocal microscopy. LNCap was used as a negative control as these cells have very low levels of CD44. For each row, the first image was the red channel from PE-Cy^{TM}5 labeled IM7. The second image was the laser images of the cells and the third image was the overlay of the first and the second. (**b**) Western blot showed the presence of significant amount of CD44 in EA.hy926 cells.

not bind strongly with FITC-HA-NP (Fig. 3a). This was explained by the fact that CD44 receptors normally existed in a quiescent state having low affinities towards HA (42, 43).

To mimic the inflammatory process common in atherosclerotic plaques, the pro-inflammatory cytokine TNF-α (10 ng/mL) was added to the culture media of EA.hy926 cells. TNF-α induces sulfation of CD44, which leads to substantial conformational changes transforming CD44 into a high affinity form for HA (42, 43). This mechanism is used in the body for recruiting inflammatory cells to plaque sites (42, 43). With TNF-α treatment, activated EA.hy926 cells exhibited significantly enhanced binding of HA-NPs (Fig. 3a). HA-NP interaction with activated EA.hy926 cells was rapid with binding observed just after 30 min incubation. The higher uptake of HA-NPs induced by TNF-α was not due to cell membrane leakiness, as either quiescent or TNF-α stimulated cells did not retain much the control NPs lacking HA coatings (Fig. 3a). These results suggest the importance of HA in modulating interactions with EA.hy926 cells.

The EA.hy926 cells were imaged by confocal microscopy upon incubation with FITC-HA-NPs. In the absence of TNF-α, there were little NPs associated with the cells as the FITC channel gave very little fluorescence (Fig. 3f). In contrast, extensive green color was evident when EA.hy926 cells were treated with TNF-α confirming the higher uptake induced by TNF-α observed in flow cytometry studies (Fig. 3b).

To demonstrate the role of CD44 in HA-NP/cell interaction, CD44 knockdown experiments were performed. EA.hy926 cells were treated with an anti-CD44 small interfering RNA (siRNA), which could bind with CD44 messenger

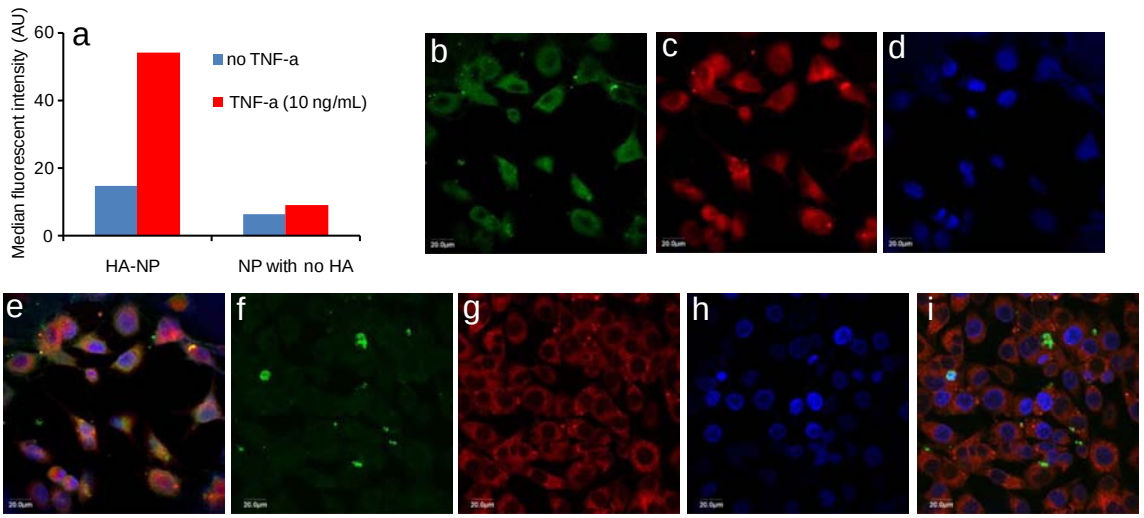

Fig. 3 (**a**) The uptake of HA-NP or NP 1 containing no HA by EA.hy926 cells with or without TNF-α treatment as measured by flow cytometry. (**b**-**e**) Confocal fluorescent microscopy images of activated EA.hy926 cells upon incubation with FITC-HA-NP. (**b**) Fluorescein channel (*green color*) showing location of the NPs; (**c**) Lysotracker red channel (*red color*) showing lysosomes; (**d**) DAPI channel (*blue color*) showing location of the nuclei; (**e**) overlay of (**b**-**d**) showing NPs were mainly in the lysosomes (*yellow color*). (**f**-**i**) Confocal fluorescent microscopy images of activated EA.hy926 cells upon incubation with NP 1. (**f**) Fluorescein channel (*green color*) showing location of the NPs; (**g**) Lysotracker red channel (*red color*) showing lysosomes; (**h**) DAPI channel (*blue color*) showing location of the nuclei; (**i**) overlay of (**f**-**h**). The scale bar is 20 mm.

RNAs leading to their cleavage. As a result, the amounts of CD44 expressed in treated cells would decrease transiently. The successful knockdown of CD44 from EA.hy926 cells was confirmed by Western blot with lower level of CD44 48 h after anti-CD44 siRNA treatment (Fig. 4a). The reduced CD44 levels correlated with reduced binding and uptake of HA-NPs in anti-CD44 siRNA treated EA.hy926 cells (Fig. 4b). In comparison, the treatment of EA.hy926 cells with a control siRNA sequence did not lead to any changes in CD44 levels or HA-NP binding (Fig. 4a,b). These results suggested that the interactions of activated endothelial cells with HA-NPs were at least partially CD44 dependent.

CD44 is known to traffic between endosomes and the cell surface. We envisioned the CD44 dependent binding could be a mechanism to internalize HA-NPs into endothelial cells. Confocal microscopy analysis of activated EA.hy926 cells showed a significant amount of green fluorescence in the cytoplasm following just 30 min incubation with FITC-HA-NPs, suggesting rapid NP uptake into the cytoplasm of the cells (Fig. 3b). The ability to internalize HA-NPs can enhance the binding capacity of the cells (thus potentially higher detection sensitivity) as cell surface binding sites can be limited. The higher uptake and accumulation of HA-NPs in these activated cells suggest that the inflammation dependent affinity switch can be utilized for plaque imaging.

With the promising *in vitro* data, we moved on to *in vivo* imaging. As a model for inflammation and plaque formation, we injured a New Zealand white rabbit's aorta using a balloon-catheter, which scraped some endothelial cells off the aorta wall surface, thus inducing inflammation in the wall. The rabbits were then fed with a high fat and high cholesterol Western diet for 4 weeks (56). The balloon catheter protocol mimics the injury by oxidized low density lipoprotein (LDL) during plaque development in humans. The inflammation was further exacerbated by the high plasma cholesterol level resulting from the diet, which was confirmed by histological analysis as evident from the large amounts of macrophages present in the plaques (Fig. S8a). Consistent with literature, high levels of CD44 were observed on the surface of vessel wall at the lumen side (Fig. S8b).

To detect plaques, HA-NPs (0.21 mg of Fe/kg of body weight corresponding to 0.006 mg Fe/mL of blood) were injected into the rabbit ear vein followed by MRI. After testing a variety of MR pulse sequences, we established a 3D Fast SPoiled Gradient Recalled (FSPGR) sequence to acquire T2* weighted images with a high spatial resolution with no spatial gaps and high signal-to-noise ratios. In this rabbit model, only modest plaques had developed with little stenosis of aorta due to the short duration of the Western diet. Consequently, 3D FSPGR T2* weighted MRI without the aid of the NPs did not reveal much abnormality in the anatomy of the descending aorta wall (Fig. 5a). However, thirty minutes after HA-NP injection, multiple areas of signal decrease (i.e., darkening) of the aorta wall in T2* weighted images were observed (Fig. 5b, Fig. S5). The signal intensities of the lumen also dropped, but the changes of lumen intensities were much smaller compared to those of the vessel walls (Fig. 5f), suggesting the NPs were concentrated in selected regions of the vessel walls.

To quantify the MR signal changes over time and minimize the background variation, the signal intensities at the plaque sites were calibrated using the mean signal intensity of the back muscle posterior to the spine. Normalization using the muscle signals was valid since no significant amounts of NPs were expected to penetrate to the muscle during the time frame of these experiments and thus muscle signal changes provided good gauges of the slight background variation between images acquired at different time points. Injection of the CD44 targeting HA-NPs resulted in 43% signal loss at the aorta wall, suggesting significant amounts of HA-NPs were bound at plaque sites (Fig. 5f). The contrast changes of the aorta wall remained for more than 17 h (Fig. 5c-f).

The importance of HA in plaque detection *in vivo* was established by several experiments. First, a competition experiment was carried out by injecting free HA into atherosclerotic rabbits followed by HA-NPs (0.21 mg of Fe/kg of body weight). No significant contrast changes in aorta wall were observed in T2* weighted images before and after NP administration (Fig. 6a-c). This was explained as free HA binds with CD44, it would compete with HA-NP for plaque binding. As a result, the amount of HA-NPs retained by

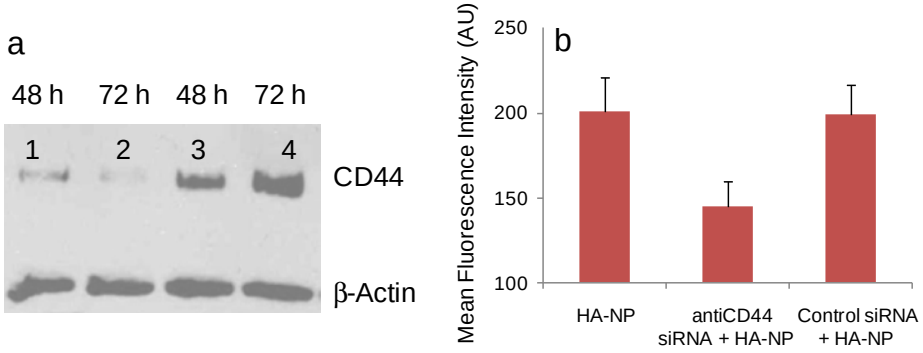

Fig. 4 (**a**) Western blot showed reduction of CD44 levels in EA.hy926 cells upon treatment with anti-CD44 siRNA for 48 h (lane 1) and 72 h (lane 2) but not the control sequence (lanes 3 and 4). (**b**) Uptake of HA-NPs by EA.hy926 cells before and after transfection with anti-CD44 siRNA as compared to that with control siRNA.

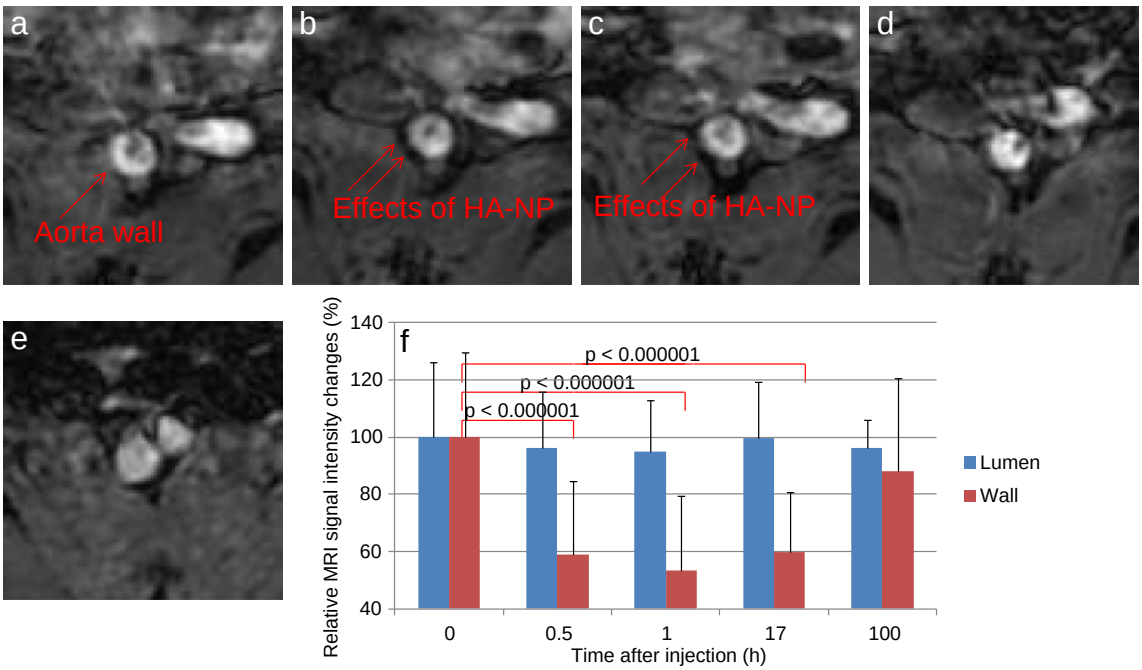

Fig. 5 *In vivo* T2* weighted MR images of the atherosclerotic rabbit aorta. (**a**) Before HA-NP injection (0 h); (**b**) 0.5 h; (**c**) 1 h; (**d**) 17 h and (**e**) 100 h after HA-NP (0.21 mg Fe/kg of body weight) injection; (**f**) Quantification of relative MRI signal intensity changes of the lumen and vessel walls of three consecutive slices at the location around that shown in images (**a**-**e**) after calibrations against signals at muscles. The pre-injection signal intensities of the lumen and the vessel wall were set as 100% respectively. Statistical analysis was performed using (*t*) test.

plaques should be much smaller with no effects on image contrasts. Next, the same dose of HA-NPs was administered to a normal rabbit without any atherosclerosis. Although decreases of lumen intensities were observed post NP administration indicating HA-NPs did enter the circulation, no darkening of the vessel wall in T2* weighted images was detected at 30 min or 1 h after injection (Fig. S6). Another control experiment was performed by testing NPs without HA in atherosclerotic rabbits (Fig. S7c,d). At the same Fe concentration of HA-NPs administered, the aorta wall did not exhibit loss of signals in T2* weighted MR images. These results collectively suggest the important role of HA on HA-NP for plaque imaging *in vivo*.

To confirm the MRI results, *ex vivo* tissue staining was performed with NPs. Tissue sections (~ 1 cm^2) were cut from aortas of both normal and atherosclerotic rabbits and incubated with HA-NPs (0.05 mg Fe/mL). After removing the unbound NP by thorough washing, the tissues were stained with Prussian blue, a specific staining method to detect ferric ions from the NP core. The artery tissue from the normal rabbit showed little blue staining, demonstrating that it did not retain HA-NPs much (Fig. 7a). On the

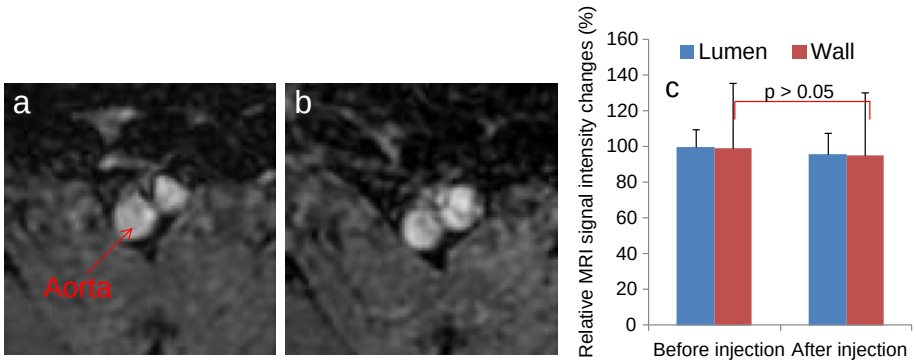

Fig. 6 Free HA inhibited the HA-NP induced contrast changes as no significant signal intensity differences were observed after injection of HA-NP following free HA administration. *In vivo* T2* weighted MR images of the aorta wall of an atherosclerotic rabbit (**a**) before injection; (**b**) 1 h after injections of free HA (5 mg/kg) and HA-NP (0.21 mg Fe/kg of body weight); (**c**) Quantification of relative MRI signal intensity changes of the lumen and vessel walls of three consecutive slices at the location around that shown in (**a**) and (**b**). The pre-injection signal intensities of the lumen and the vessel wall were set as 100% respectively. Statistical analysis was performed using *t* test.

contrary, HA-NPs bound strongly to the atherosclerotic plaque areas as detected by Prussian blue (Fig. 7b,c). Addition of free HA (2 mg/mL) during HA-NP incubation completely blocked HA-NP binding to plaques. Consistent with the *in vivo* results, NPs without HA functionalization did not stain the atherosclerotic tissue, confirming that the HA-NP/plaque tissue interactions were HA dependent (Fig. 7d). The rabbit aortas were then imaged *ex vivo* using a T2* weighted MR sequence following HA-NP incubation and thorough washing. Consistent with the Prussian blue staining results, as the normal tissue did not retain much HA-NPs, it appeared bright with very little darkening in T2* weighted MR images (Fig. 7e). In contrast, significant darkening of the plaque tissue was observed after HA-NP incubation (Fig. 7f). The dark area was only present at the lumen side of the aorta wall consistent with the plaque location.

An important consideration of contrast agent development is that the agent should not cause serious side effects to the host. The HA-NPs did not affect the viability of cells in cell viability assays of multiple cell lines including human macrophages and cancer cells (48–50). The biocompatibility of the HA-NPs was evaluated *in vivo*. Blood was drawn from rabbits 1 h and 4 days after HA-NP administration at the imaging dose to assess acute effects of the NPs. The complete blood count (CBC) test and the comprehensive blood chemistry panel were performed on the blood, and all the parameters evaluated were in normal range (Table S1). Most noteworthy were the negligible changes in alkaline phosphatase, aspartate aminotransferase and alanine aminotransferase levels (markers for liver function) and the white blood cell count (marker for inflammation) suggesting negligible acute toxicities. Typically, liver and kidney are the major organs involved in NP clearance. The rabbits were sacrificed 2 days post injection and their organs were extracted. Histopathological analysis of rabbit liver, kidney and spleen were performed, which showed no signs of toxicities (Fig. S9). These results suggest the high biocompatibilities of the HA-NPs under the parameters evaluated.

DISCUSSION

CD44 is a cell adhesion molecule expressed on the surface of a variety of cells, which can exist in three forms, i.e., low affinity form, high affinity form induced by inflammation, and constitutive high affinity form. On the vast majority of normal cells, CD44 is present at the low affinity state with little interactions with HA (43). The constitutive high affinity form of CD44 is expressed on many cancer cells (57). As a result, HA functionalized nanomaterials have been successfully developed to target CD44 expressing cancer cells and to selectively deliver drugs for cancer treatment (58–62). In comparison, the interactions of HA-NP with atherosclerotic plaques have not been extensively investigated. We found that vascular endothelial cells could be induced to interact strongly with HA-NP upon stimulation by the inflammatory signal cytokine TNF-α. Siegelman and coworkers reported that upon TNF-α treatment, endothelial cells could bind with HA more strongly, although the overall level of cell surface CD44 remained unchanged (40). This was attributed to the activation of CD44 to its HA-binding form. Our results are consistent with this report. The enhanced HA affinity of endothelial cells in inflammation can facilitate leukocyte recruitment in response to injury in the body and the HA-NP can mimic this process.

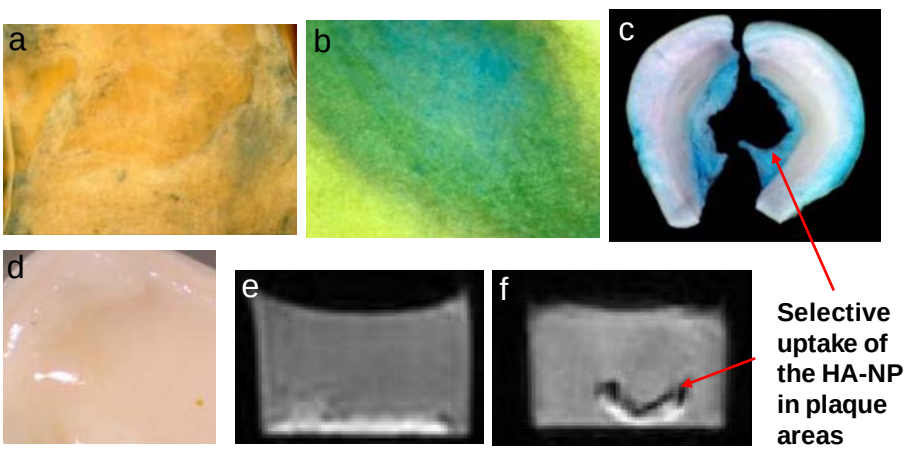

Fig. 7 (**a**-**f**) Images of rabbit aorta incubated with NPs after removal of unbound particles. (**a**) Normal aorta tissue and (**b**) atherosclerotic tissue incubated with HA-NP after Prussian blue stain and nuclear fast red counterstaining; (**c**) Cross section of the atherosclerotic tissue after Prussian blue stain; (**d**) Atherosclerotic tissue incubated with NP 1 containing no HA after Prussian blue stain and nuclear fast red counterstaining. T2* weighted MR images of (**e**) the normal tissue and (**f**) the atherosclerotic tissue after HA-NP incubation.

It is known that endogenous HA has molecular weights ranging from 10 kDa to 10 MDa (39). CD44 is a monomeric protein containing a single HA binding link module, which can accommodate a HA oligosaccharide up to hexasaccharide in length (63). Although high molecular weight HA has enhanced avidity to cell surface CD44 due to simultaneous interactions with multiple copies of CD44, HA oligosaccharide longer than decasaccharide has been shown to be able to compete with high molecular weight HA for cellular binding (64, 65). Moreover, HA oligosaccharides and low molecular weight HA have been immobilized onto liposomes and NPs to target CD44 expressing cancer cells (66–68). One advantage of low molecular HA compared to their high molecular weight counterpart is the ease in separating unreacted HA from the HA-NPs. Based on these considerations, we selected low molecular weight HA as our targeting ligand. The HA on our HA-NPs can effectively bind with CD44 as demonstrated by ELISA and cellular binding studies.

HA coated nanomaterials have been shown to be internalized inside the cells through CD44 mediated endocytosis from cholesterol rich lipid rafts (69–71). The CD44 dependence was confirmed by competition experiments. When CD44 expressing cells were incubated with the anti-CD44 mAb MEM-85, a mAb known to compete with HA binding (72), the amount of bound HA-NP significantly decreased (48). Addition of free HA together with HA-NPs also significantly reduced the binding of HA-NPs, presumably due to the competitive binding of free HA with CD44. Our observation that the knockdown of CD44 by siRNA reduced HA-NP binding further supports the roles of CD44.

As discussed in the Introduction, SPIONs have been investigated as a T2* based contrast agent for plaque imaging. However, due to the non-targeted nature of the SPIONs for macrophage uptake, high concentrations of SPIONs were typically utilized to ensure sufficient NPs reached plaque sites (12–15). As a result, the lumen of the aorta appeared very dark in T2* weighted images right after injection, rendering it impossible to distinguish vessel wall from the lumen and to visualize vessel wall contrast changes. To detect plaques and inflammation, imaging was commonly carried out at least 1 day after injection so that NPs in the lumen were cleared sufficiently. The delay between contrast agent administration and imaging can be a serious hurdle for patient compliance and the wide clinical application of SPIONs for plaque detection.

In our study, by targeting cell surface receptor CD44, the cellular uptake of HA-NPs by plaque residing cells such as vascular endothelial cells can be significantly enhanced. This in turn enables us to lower the amount of the contrast agent needed. Several dosages (0.21–3 mg/kg body weight) were evaluated *in vivo*. The 0.21 mg of Fe/kg of body weight dose was selected since it was a low dose yet significant difference in plaque contrast before and after HA-NP administration was observed. As a result of the low dosage, the concentration of the HA-NPs in blood circulation was low even right after probe administration and the lumen and the vessel wall were readily distinguished in T2* weighted MRI. Furthermore, HA-NPs could rapidly bind with the CD44 on cell surface, which allowed us to observe contrast changes of vessel wall right after injection. This bodes well for potential clinical applications.

In addition to HA-NPs, we examined the NPs without HA functionalization. Although this type of non-targeted NPs have been used for plaque imaging (12–15), no significant contrast changes were observed in plaques after injection in our study. This was not due to slow kinetics of binding as imaging at 10 min or 1 day did not show much difference. We attributed the lack of contrast change to the much lower concentration of NPs employed compared to the traditional studies. Although *ex vivo* Prussian blue staining of plaque tissue upon incubation with NPs without HA exhibited some blue coloration (Fig. 6a), the amount of NPs accumulated in plaque was presumably not sufficient to cause observable contrast changes in MRI.

The iron oxide based NPs are shown to be generally safe in animals and humans (17, 73, 74). However, recently some concerns have been raised regarding the possible side effects of these particles (18). As toxicity is a function of concentration, the much lower dose of the HA-NPs utilized in our study coupled with their high biocompatibilities can potentially alleviate the toxicity concern.

CONCLUSION

Although previously unexplored, CD44 can serve as a biomarker for the imaging of atherosclerotic plaques. Taking advantage of the inflammation induced affinity switch of CD44 to HA-NPs, significant enhancement in cellular uptake of HA-NPs was achieved, which enabled us to detect atherosclerotic plaques by MRI. CD44 targeting allowed plaque imaging without much delay as well as the usage of HA-NPs at a lower dose compared to the traditional non-targeted SPION contrast agents. This highlights the advantages of active targeting of vascular cell surface receptors. Studies are ongoing to further enhance the detection sensitivity of plaques using the CD44-targeting NPs and to longitudinally monitor plaque development processes.

ACKNOWLEDGMENTS AND DISCLOSURES

Mohammad H. El-Dakdouki, Kheireddine El-Boubbou and Medha Kamat contributed equally to this work. We would like to thank the Department of Radiology, Michigan State University for the very generous support towards access of the MRI scanner.

REFERENCES

1. Libby P. Inflammation in atherosclerosis. Nature. 2002;420:868–74.
2. Sanz J, Fayad ZA. Imaging of atherosclerotic cardiovascular disease. Nature. 2008;451:953–7.
3. Canet-Soulas E, Letourneur D. Biomarkers of atherosclerosis and the potential of MRI for the diagnosis of vulnerable plaque. Magn Reson Mater Phy. 2007;20:129–42.
4. Briley-Saebo KC, Mulder WJM, Venkatesh Mani V, Hyafil F, Amirbekian V, Aguinaldo JGS, *et al.* Magnetic resonance imaging of vulnerable atherosclerotic plaques: current imaging strategies and molecular imaging probes. J Mag Res Imag. 2007;26:460–79.
5. Jaffer FA, Libby P, Weissleder R. Molecular and cellular imaging of atherosclerosis. Emerging applications. J Am Coll Cardiol. 2006;47:1328–38.
6. Amirbekian V, Lipinski MJ, Briley-Saebo KC, Amirbekian S, Aguinaldo JGS, Weinreb DB, *et al.* Detecting and assessing macrophages *in vivo* to evaluate atherosclerosis noninvasively using molecular MRI. Proc Nat Acad Sci U S A. 2007;104:961–6.
7. Nair SA, Kolodziej AF, Bhole G, Greenfield MT, McMurry TJ, Caravan P. Monovalent and bivalent fibrin-specific MRI contrast agents for detection of thrombus. Angew Chem Int Ed. 2008;47:4918–21.
8. Winter PM, Caruthers SD, Zhang H, Williams TA, Wickline SA, Lanza GM. Antiangiogenic synergism of integrin-targeted Fumagillin nanoparticles and atorvastatin in atherosclerosis. JACC: Cardiovasc Imaging. 2008;1:624–34.
9. Winter PM, Neubauer AM, Caruthers SD, Harris TD, Robertson JD, Williams TA, *et al.* Endothelial a_vb_3 integrin-targeted Fumagillin nanoparticles inhibit angiogenesis in atherosclerosis. Arterioscler Thromb Vasc Biol. 2006;26:2103–9.
10. Bhave G, Lewis JB, Chang SS. Association of gadolinium based magnetic resonance imaging contrast agents and nephrogenic systemic fibrosis. J Urol. 2008;180:830–5.
11. Thorek DLJ, Chen AK, Czupryna J, Tsourkas A. Superparamagnetic iron oxide nanoparticle probes for molecular imaging. Ann Biomed Eng. 2006;34:23–38.
12. Sigovan M, Boussel L, Sulaiman A, Sappey-Marinier D, Alsaid H, Desbleds-Mansard C, *et al.* Rapid-clearance iron nanoparticles for inflammation imaging of atherosclerotic plaque: initial experience in animal model. Radiology. 2009;252:401–9.
13. Morris JB, Olzinski AR, Bernard RE, Aravindhan K, Mirabile RC, Boyce R, *et al.* p38 MAPK inhibition reduces aortic ultrasmall superparamagnetic iron oxide uptake in a mouse model of atherosclerosis. MRI assessment. Arterioscler Thromb Vasc Biol. 2008;28:265–71.
14. Durand E, Raynaud JS, Bruneval P, Brigger I, Al Haj Zen A, Mandet C, *et al.* Magnetic resonance imaging of ruptured plaques in the rabbit with ultrasmall superparamagnetic particles of iron oxide. J Vasc Res. 2007;44:119–28.
15. Ruehm SG, Corot C, Vogt P, Kolb S, Debatin JF. Magnetic resonance imaging of atherosclerotic plaque with ultrasmall superparamagnetic particles of iron oxide in hyperlipidemic rabbits. Circulation. 2001;103:415–22.
16. Hyafil F, Laissy J-P, Mazighi M, Tchétché D, Louedec L, Adle-Biassette H, *et al.* Ferumoxtran-10–Enhanced MRI of the hypercholesterolemic rabbit aorta relationship between signal loss and macrophage infiltration. Arterioscler Thromb Vasc Biol. 2006;26:176–81.
17. Weissleder R, Stark DD, Engelstad BL, Bacon BR, Compton CC, White DL, *et al.* Superparamagnetic iron oxide: pharmacokinetics and toxicity. Am J Roentgenol. 1989;152:167–73.
18. Singh N, Kenkins GJS, Asadi R, Doak SH. Potential toxicity of Superparamagnetic Iron Oxide Nanoparticles (SPION). Nano Rev. 2010;1:5358.
19. McAteer MA, Schneider JE, Ali ZA, Warrick N, Bursill CA, Von zur Muhlen C, *et al.* Magnetic resonance imaging of endothelial adhesion molecules in mouse atherosclerosis using dual-targeted microparticles of iron oxide. Arterioscler Thromb Vasc Biol. 2008;28:77–83.
20. Nahrendorf M, Jaffer FA, Kelly KA, Sosnovik DE, Aikawa E, Libby P, *et al.* Noninvasive vascular cell adhesion Molecule-1 imaging identifies inflammatory activation of cells in atherosclerosis. Circulation. 2006;114:1504–11.
21. Kelly KA, Allport JR, Tsourkas A, Shinde-Patil VR, Josephson L, Weissleder R. Detection of vascular adhesion molecule-1 expression using a novel multimodal nanoparticle. Circ Res. 2005;96:327–36.
22. Smith BR, Heverhagen J, Knopp M, Schmalbrock P, Shapiro J, Shiomi M, *et al.* Localization to atherosclerotic plaque and biodistribution of biochemically derivatized Superparamagnetic Iron Oxide Nanoparticles (SPIONs) contrast particles for Magnetic Resonance Imaging (MRI). Biomed Microdevices. 2007;9:719–27.
23. Sosnovik DE, Schellenberger EA, Nahrendorf M, Novikov MS, Matsui T, Dai G, *et al.* Magnetic resonance imaging of cardiomyocyte apoptosis with a novel magneto-optical nanoparticle. Magn Reson Med. 2005;54:718–24.
24. Tu C, Ng TSC, Sohi HK, Palko HA, House A, Jacobs RE, *et al.* Receptor-targeted iron oxide nanoparticles for molecular MR imaging of inflamed atherosclerotic plaques. Biomaterials. 2011;32:7209–16.
25. Radermacher KA, Beghein N, Boutry S, Laurent S, Elst LV, Muller RN, *et al. In vivo* detection of inflammation using pegylated iron oxide particles targeted at E-selectin a multimodal approach using MR Imaging and EPR Spectroscopy. Invest Radiol. 2009;44:398–404.
26. Kang HW, Josephson L, Petrovsky A, Weissleder R, Bogdanov A. Magnetic resonance imaging of inducible E-selectin expression in human endothelial cell culture. Bioconjugate Chem. 2002;13:122–7.
27. Crowther MA. Pathogenesis of Atherosclerosis. Hematol. 2005:436–41.
28. Zhao L, Lee E, Zukas AM, Middleton MK, Kinder M, Acharya PS, *et al.* CD44 expressed on both bone marrow–derived and non–bone marrow–derived cells promotes atherogenesis in ApoE-deficient mice. Arterioscler Thromb Vasc Biol. 2008;28:1283–9.
29. Zhao L, Hall JA, Levenkova N, Lee E, Middleton MK, Zukas AM, *et al.* CD44 regulates vascular gene expression in a proatherogenic environment. Arterioscler Thromb Vasc Biol. 2007;27:886–92.
30. Cuff CA, Kothapalli D, Azonobi I, Chun S, Zhang Y, Belkin R, *et al.* The adhesion receptor CD44 promotes atherosclerosis by mediating inflammatory cell recruitment and vascular cell activation. J Clin Invest. 2001;108:1031–40.
31. Hägg D, Sjöberg S, Hultén LM, Fagerberg B, Wiklund O, Rosengren A, *et al.* Augmented levels of CD44 in macrophages from atherosclerotic subjects: a possible IL-6–CD44 feedback loop? Atherosclerosis. 2007;190:291–7.
32. McKee CM, Penno MB, Cowman M, Burdick MD, Strieter RM, Bao C, *et al.* Hyaluronan (HA) fragments induce chemokine gene expression in alveolar macrophages: the role of HA size and CD44. J Clin Invest. 1996;98:2403–13.
33. Jain M, He Q, Lee W-S, Kashiki S, Foster LC, Tsai J-C, *et al.* Role of CD44 in the reaction of vascular smooth muscles cells to arterial wall injury. J Clin Invest. 1996;97:596–603.
34. Puré E, Cuff CA. A crucial role for CD44 in inflammation. Trends Mol Med. 2001;7:213–21.
35. Krettek A, Sukhova GK, Schönbeck U, Libby P. Enhanced expression of CD44 variants in human atheroma and abdominal aortic aneurysm. Possible role for a feedback loop in endothelial cells. Am J Pathol. 2004;165:1571–81.
36. Kolodgie FD, Burke AP, Farb A, Weber DK, Kutys R, Wight TN, *et al.* Differential accumulation of proteoglycans and hyaluronan in

culprit lesions. Insights into plaque erosion. Arterioscler Thromb Vasc Biol. 2002;22:1642–8.
37. Kinscherf R, Wagner M, Kamencic H, Bonaterra GA, Hou D, Schiele RA, *et al.* Characterization of apoptotic macrophages in atheromatous tissue of humans and heritable hyperlipidemic rabbits. Atherosclerosis. 1999;144:33–9.
38. Ponta H, Sherman L, Herrlich PA. CD44: from adhesion molecules to signalling regulators. Nature Rev Mol Cell Biol. 2003;4:33–45.
39. Lapcik Jr L, Lapcik L, De Smedt S, Demeester J, Chabrecek P. Hyaluronan: preparation, structure, properties, and applications. Chem Rev. 1998;98:2663–84.
40. Nandi A, Estess P, Siegelman MH. Hyaluronan anchoring and regulation on the surface of vascular endothelial cells is mediated through the functionally active form of CD44. J Biol Chem. 2000;275:14939–48.
41. Levesque MC, Haynes BF. *In vitro* culture of human peripheral blood monocytes induces hyaluronan binding and up-regulates monocyte variant CD44 lsoform expression. J Immunol. 1996;156:1557–65.
42. Brown KL, Maiti A, Johnson P. Role of sulfation in CD44-mediated hyaluronan binding induced by inflammatory mediators in human CD14 peripheral blood monocytes. J Immunol. 2001;167:5367–74.
43. Maiti A, Maki G, Johnson P. TNF-alpha induction of CD44-mediated leukocyte adhesion by sulfation. Science. 1998;282:941–3.
44. DeGrendele HC, Estess P, Siegelman MH. Requirement for CD44 in activated T cell extravasation into an inflammatory site. Science. 1997;278:672–5.
45. DeGrendele HC, Estess P, Picker LJ, Siegelman MH. CD44 and its ligand hyaluronate mediate rolling under physiologic flow: a novel lymphocyte-endothelial cell primary adhesion pathway. J Exp Med. 1996;183:1119–30.
46. El-boubbou K, Huang X. Glyco-nanomaterials: translating insights from the "Sugar-Code" to biomedical applications. Curr Med Chem. 2011;18:2060–78.
47. Palmacci S, Josephson L, Groman EV. Synthesis of Polysaccharide Covered Superparamagnetic Oxide Colloids. US Patent WO/1995/005669. 1995.
48. Kamat M, El-boubbou K, Zhu D, Lansdell T, Lu X, Li W, *et al.* Hyaluronic acid immobilized magnetic nanoparticles for active targeting and imaging of macrophages. Bioconjugate Chem. 2010;21:2128–35.
49. El-Dakdouki MH, El-boubbou K, Zhu DC, Huang X. A simple method for the synthesis of hyaluronic acid coated magnetic nanoparticles for highly efficient cell labelling and *in vivo* imaging. RSC Adv. 2011;1:1449–52.
50. El-Dakdouki MH, Zhu DC, El-boubbou K, Kamat M, Chen J, Li W, *et al.* Development of multifunctional hyaluronan-coated nanoparticles for imaging and drug delivery to cancer cells. Biomacromolecules. 2012;13:1144–51.
51. Alexis F, Pridgen E, Molnar LK, Farokhzad OC. Factors affecting the clearance and biodistribution of polymeric nanoparticles. Mol Pharmaceutics. 2008;5:505–15.
52. Davignon J, Ganz P. Role of endothelial dysfunction in atherosclerosis. Circulation. 2004;109:III27–32.
53. Bouïs D, Hospers GAP, Meijer C, Molema G, Mulder NH. Endothelium *in vitro*: a review of human vascular endothelial cell lines for blood vessel-related research. Angiogenesis. 2001;4:91–102.
54. Hurt EM, Kawasaki BT, Klarmann GJ, Thomas SB, Farrar WL. $CD44^{+}CD24^{-}$ prostate cells are early cancer progenitor/stem cells that provide a model for patients with poor prognosis. Br J Cancer. 2008;98:756–65.
55. Dhir R, Gau JT, Krill D, Bastacky S, Bahnson RR, Cooper DL, *et al.* CD44 expression in benign and neoplastic human prostates. Mol Diagn. 1997;2:197–204.
56. Yanni AE. The laboratory rabbit: an animal model of atherosclerosis research. Lab Animals. 2004;38:246–56.
57. Cichy J, Puré E. The liberation of CD44. J Cell Biol. 2003;161:839–43.
58. El-Dakdouki MH, Huang X. Biological applications of hyaluronic acid functionalized nanomaterials. In X. Huang and J. Barchi (eds.), Petite and Sweet: Glyco-nanotechnology as a bridge to new medicines, ACS Symposium Series, 2011, pp. 181–213 and references cited therein.
59. Platt VM, Szoka Jr FC. Anticancer therapeutics: targeting macromolecules and nanocarriers to hyaluronan or CD44, a hyaluronan receptor. Mol Pharmaceutics. 2008;5:474–86. references cited therein.
60. Choi KY, Min KH, Yoon HY, Kim K, Park JH, Kwon IC, *et al.* PEGylation of hyaluronic acid nanoparticles improves tumor targetability *in vivo*. Biomaterials. 2011;32:1880–9.
61. Rivkin I, Cohen K, Koffler J, Melikhov D, Peer D, Margalit R. Paclitaxel-clusters coated with hyaluronan as selective tumor-targeted nanovectors. Biomaterials. 2010;31:7106–14.
62. Bachar G, Cohen K, Hod R, Feinmesser R, Mizrachi A, Shpitzer T, *et al.* Hyaluronan-grafted particle clusters loaded with Mitomycin C as selective nanovectors for primary head and neck cancers. Biomaterials. 2011;32:4840–8.
63. Banerji S, Wright AJ, Noble M, Mahoney DJ, Campbell ID, Day AJ, *et al.* Structures of the CD44–hyaluronan complex provide insight into a fundamental carbohydrate protein interaction. Nat Struc Mol Biol. 2007;14:234–9.
64. Tammi R, Rilla K, Pienimäki JP, MacCallum D, Hogg M, Luukkonen M, *et al.* Hyaluronan enters keratinocytes by a novel endocytic route for catabolism. J Biol Chem. 2001;276:35111–22.
65. Tammi R, MacCallum D, Hascall VC, Pienimäki JP, Hyttinen M, Tammi M. Hyaluronan bound to CD44 on keratinocytes is displaced by hyaluronan decasaccharides and not hexasaccharides. J Biol Chem. 1998;273:28878–88.
66. Eliaz RE, Nir S, Marty C, Szoka Jr FC. Determination and modeling of kinetics of cancer cell killing by doxorubicin and doxorubicin encapsulated in targeted liposomes. Cancer Res. 2004;64:711–8.
67. Luo Y, Bernshaw NJ, Lu ZR, Kopecek J, Prestwich GD. Targeted delivery of doxorubicin by HPMA copolymer-hyaluronan bioconjugates. Pharm Res. 2002;19:396–402.
68. Eliaz RE, Szoka Jr FC. Liposome-encapsulated doxorubicin targeted to CD44: a strategy to kill CD44-overexpressing tumor cells. Cancer Res. 2001;61:2592–601.
69. Lee JL, Wang MJ, Sudhir PR, Chen JY. CD44 engagement promotes matrix-derived survival through the CD44-Src-Integrin axis in lipid rafts. Mol Cell Biol. 2008;28:5710–23.
70. Thankamony SP, Knudson W. Acylation of CD44 and its association with lipid rafts are required for receptor and hyaluronan endocytosis. J Biol Chem. 2006;281:34601–9.
71. Qhattal HSS, Liu X. Characterization of CD44-mediated cancer cell uptake and intracellular distribution of hyaluronan-grafted liposomes. Mol Pharmaceutics. 2011;8:1233–46.
72. Ahrens T, Assmann V, Fieber C, Termeer CC, Herrlich P, Hofmann M, *et al.* CD44 is the principal mediator of hyaluronic-acid-induced melanoma cell proliferation. J Invest Dermatol. 2001;116:93–101.
73. Tang TY, Howarth SPS, Miller SR, Graves MJ, Patterson AJ, U-King-Im J-M, *et al.* The ATHEROMA (Atorvastatin Therapy: Effects on Reduction of Macrophage Activity) Study: evaluation using ultrasmall superparamagnetic iron oxide-enhanced magnetic resonance imaging in carotid disease. J Am Coll Card. 2009;53:2039–50.
74. Fayad ZA, Razzouk L, Briley-Saebo KC, Mani V. Iron oxide magnetic resonance imaging for atherosclerosis therapeutic evaluation. Still "Rusty?". J Am Coll Card. 2009;53:2051–2.